



Article

Geochemistry and Mineralogy of Basalts from the South Mid-Atlantic Ridge (18.0°–20.6°S): Evidence of a Heterogeneous Mantle Source

Yun Zhong^{1,2}, Weiliang Liu^{1,2,*} , Zhilei Sun^{1,2}, Chris Yakymchuk³ , Kefa Ren⁴,
Jinnan Liu^{1,5,6}, Wei Li^{1,5,6}, Yaoliang Ma^{1,5,6} and Bin Xia^{1,5,6}

¹ School of Marine Sciences, Sun Yat-sen University, Guangzhou 510006, China;

zhongy73@mail.sysu.edu.cn (Y.Z.); zhileisun@yeah.net (Z.S.); liujn27@mail2.sysu.edu.cn (J.L.);

liwei237@mail2.sysu.edu.cn (W.L.); mayliang@mail2.sysu.edu.cn (Y.M.); xiabin08@outlook.com (B.X.)

² The Key Laboratory of Gas Hydrate, Ministry of Natural Resources, Qingdao Institute of Marine Geology, Qingdao 266071, China

³ Department of Earth and Environmental Sciences, University of Waterloo, Waterloo, ON N2L 3G1, Canada; chris.yakymchuk@uwaterloo.ca

⁴ School of Earth Sciences, Chengdu University of Technology, Chengdu 610059, China; renkefa06@cdut.cn

⁵ Guangdong University Key Laboratory of Offshore Oil Exploration and Development/Guangdong Provincial Key Laboratory of Marine Resources and Coastal Engineering, School of Marine Sciences, Sun Yat-sen University, Guangzhou 510006, China

⁶ Southern Laboratory of Ocean Science and Engineering (Zhuhai, Guangdong), Zhuhai 519000, China

* Correspondence: liuweil@mail.sysu.edu.cn

Received: 27 September 2019; Accepted: 24 October 2019; Published: 27 October 2019



Abstract: The South Mid-Atlantic Ridge is a typical slow-spreading ridge that represents a modern example to understand mantle composition and the evolution of mid-ocean ridge magmatism. In this paper, we investigate basalt samples dredged from four locations along the South Mid-Atlantic Ridge ranging from 18.0° to 20.6°S. The basalts belong to the tholeiitic series and exhibit normal mid-ocean ridge basalt (N-MORB) geochemical features with variable enrichments of Rb, Th, U, and Pb and depletions of Ba and Sr relative to primitive mantle. Some samples have negative Nb–Ta anomalies whereas others have positive Na–Ta anomalies to average N-MORBs. Plagioclase phenocrysts, microphenocrysts, and microlites occur in the in the matrix; phenocrysts and microphenocrysts are bytownite and labradorite in composition. Olivine phenocrysts are forsterite (Fo87 to Fo96). Chemical zoning in phenocrysts are interpreted to record crystal fractionation and magma mixing. Cores of plagioclase phenocrysts have higher anorthite values (An72–83) and estimated crystallization temperatures (~1180–1240 °C) that may suggest a xenocrystic origin. The lower anorthite proportions of rims of plagioclase phenocrysts (An65–71) and microphenocrysts (An54–72) yield lower estimated crystallization temperatures of ~1090–1120 °C and ~980–1060 °C, respectively. Rims of plagioclase phenocrysts and microphenocrysts may be generated in different environments such as magma chambers or magma channels, respectively. The basalt samples probably originated from partial melting of a depleted mantle spinel lherzolite source with a minor contribution of enriched materials possibly derived from the Saint Helena plume and subcontinental lithospheric mantle in the asthenosphere. Variable compositions of the basalt samples suggest heterogeneous mantle that includes depleted and enriched components at the South Mid-Atlantic Ridge between 18.0°–20.6°S.

Keywords: basalt; mineralogy; geochemistry; petrogenesis; South Mid-Atlantic Ridge

1. Introduction

Mid-ocean ridges are crucial sites for the growth of oceanic crust and represent divergent plate boundaries that connect a modern globally operating network of plate tectonics. Mid-ocean ridge basalts (MORB) constitute the dominant volcanic rock type generated on modern Earth and are derived from partial melting of the upper mantle along mid-ocean ridges [1]. Previous studies have demonstrated the geochemistry and mineralogy of MORB samples provides fundamental information about the composition and evolution of the mantle, mantle plume–ridge interaction, formation of oceanic crust, and the tectonic evolution of oceanic plates (e.g., [1–6]).

The genesis of MORB includes partial melting of the mantle source and migration of the magma upwards towards the surface before emplacement on or near the sea floor; genetic models are well established (e.g., [3,6–13]). A key factor in the genesis of MORB is the rate of spreading at mid-ocean ridges (e.g., [3,6,7,9,10,14–17]). Variable spreading rates affect melt supply, magma chamber geometries, fractional crystallization, degrees of partial melting, and the thickness of the new oceanic crust, which influence the mineral assemblages, mineral zoning, and compositions of MORB (e.g., [5,6,9,11,13,15,18–23]). However, the differences between MORB volcanism in fast and slow spreading ridges require further study (e.g., [12,13,18,24–31]) and are crucial for understanding modern ocean ridge spreading and how this process may have been different in the early Earth where spreading rates may have been even more variable [32].

The Mid-Atlantic Ridge is a typical example of a slow-spreading mid-ocean ridge, and basalt samples from this ridge have been used to investigate mantle heterogeneity and ridge–plume interaction at a typical modern slow-spreading ridge (e.g., [12,13,26,29,31,33–36]). Some work has been carried out in the South Mid-Atlantic Ridge (SMAR) (e.g., [12,13,25,26,28–31,37]). Based on whole-rock major and trace element as well as Sr–Nd–Pb isotopic compositions, Skolotnev et al. proposed that MORBs from the SMAR (19°–20°S) were derived from heterogeneous mantle related to mixing of depleted mantle (DM) materials with the high U/Pb mantle (HIMU)-type components [28]. Similarly, Turner et al. suggested that the SMAR basalts originated from a heterogeneous source probably composed of spinel peridotite and recycled mafic rocks based on the ^{238}U – ^{230}Th – ^{226}Ra disequilibria of MORBs from the SMAR at 5°–11°S [30]. In addition, based on the Sr–Nd–Pb isotope analyses of Mid-Atlantic Ridge basalt glasses from 3°S to 46°S, Fontignie and Schilling suggested that basalt compositions reflect mantle plume–ridge interaction in this region in the South Atlantic [26]. Qi reported whole-rock major and trace element and mineralogical (olivine, plagioclase) compositions of basalt from the SMAR at 18°S and proposed that these rocks were influenced by the Ascension hotspot [13]. However, based on the mineralogical and Sr–Nd isotopic as well as major and trace element characteristics of basalts from SMAR at 19°S, Zhang proposed that these basalts originated from a depleted mantle source (spinel lherzolite) with negligible ridge–plume interaction [12].

Due to the variable interpretations on the influence of enriched mantle and ridge–plume interactions on the composition of basalts from the SMAR, we provide new geochemical and mineral chemical data of basalts dredged from the SMAR at 18.0° to 20.6°S (Table 1) near the Saint Helena Islands (Figure 1). Using our new results and those of previous studies, this study aims to provide a detailed genetic model for basalts from the SMAR at 18.0°–20.6°S that will further our understanding of mantle composition and heterogeneity along the South Mid-Atlantic Ridge.

Table 1. Sample dredged locations and depths.

Sample	Latitude	Longitude	Depths (m)	Rock Type
SA1 series	18.03876°S	12.85351°W	3312	basalt
SA2 series	18.02350°S	12.91643°W	3386	basalt
SA3 series	20.57449°S	11.64572°W	3302	basalt
SA4 series	18.70782°S	12.67380°W	2386	basalt

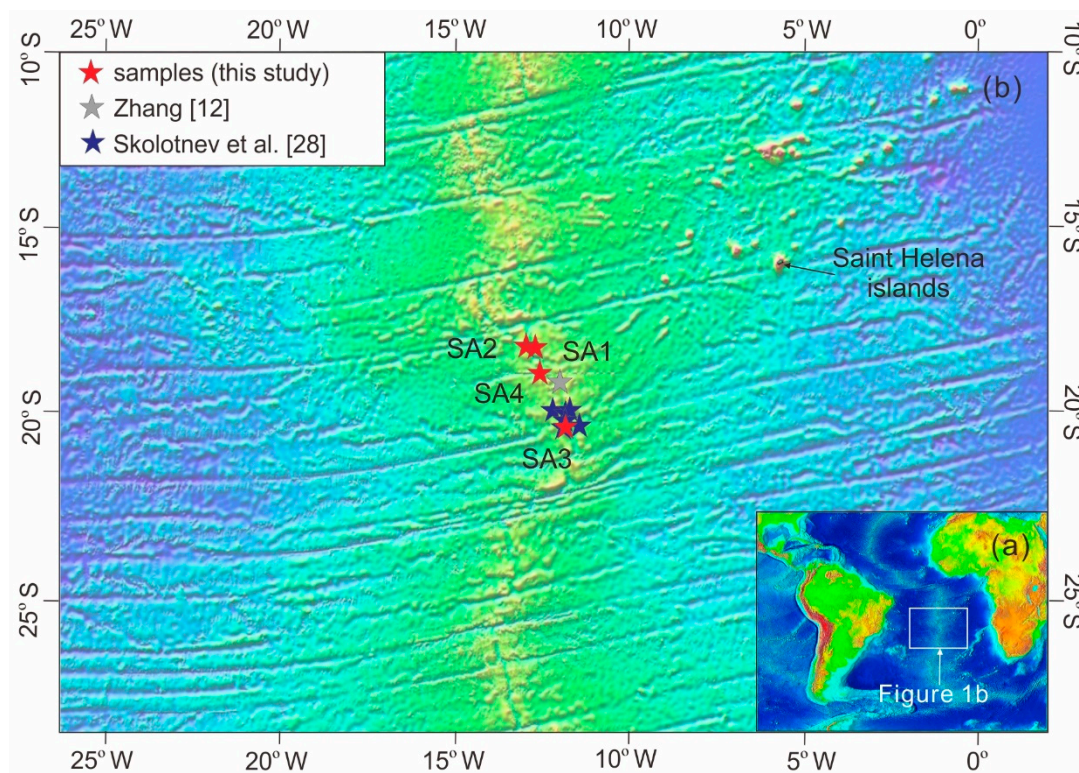


Figure 1. Map of the South Atlantic Mid-Ocean Ridge showing the locations of the dredged basalts analyzed in this study (map taken from [37]).

2. Geological Background and Sample Descriptions

The separation of Africa from South America and the opening of the South Atlantic Ocean probably happened in the Early Cretaceous following the breakup of Gondwana (e.g., [38–40]). Before and during the initial rifting stage (Early Jurassic), southern Gondwana was bounded on the Pacific side by an active subduction zone (see [41], and references therein). Previous studies proposed that the opening of the South Atlantic Ocean was related to subduction of the Pacific Ocean beneath Gondwana [41,42] or, alternatively, to two mantle plumes that have present-day positions near the oceanic islands of Saint Helena and Tristan da Cunha [43,44].

The Mid-Atlantic Ridge extends from 87°N to 54°S and accounts for ~40% of the total length of ocean ridges on Earth and its average width (1000–1300 km) represents one-third of the width of the Atlantic Ocean (e.g., [12,13]). Oceanic ridges can be divided into fast- (~80–180 mm yr⁻¹), intermediate- (~55–70 mm yr⁻¹), slow- (<55 mm yr⁻¹), and ultraslow (<12 mm yr⁻¹)-spreading types, each with different morphologic characteristics [20]. The average spreading rate of the Mid-Atlantic Ridge is ~30 mm yr⁻¹ [13], thus it is considered as a slow-spreading ridge. Generally, the Mid-Atlantic Ridge has been divided into the South Mid-Atlantic Ridge (SMAR) and the North Mid-Atlantic Ridge (NMAR), separated by the Romanche Trench near the equator [13]. Both of them show similarities in expansion rate, ridge axis morphology, and lithospheric structures [45]. The graben axis of the SMAR is relatively wide and is controlled by normal faults on both sides; several volcanic centers align into a volcanic ridge within this lenticular graben [12]. Due to the influences of transform faults, the SMAR is divided into many relatively independent sections that resemble other slow-spreading mid-ocean ridges. The main types of rocks in the SMAR are basalts as well as local serpentine, peridotite, pyroxenite, and gabbro [13]. Mineralogical and geochemical data of SMAR basalts and seismic tomography suggest that mantle plume–ridge interaction occurred along the SMAR at 3°–46°S (e.g., [13,26,28,46]), which resulted in basalts that record variable source characteristics. For example, recycled mafic rocks were proposed for the generation of basalt at 5°–11°S along the SMAR [30], HIMU-type components were invoked for basalt at 19°–20°S [28], delamination of continental lower crust was proposed for basalts at

48.5°–49.2°S [26], and remnant subcontinental lithospheric components embedded in the oceanic upper mantle (by the delamination of subcontinental lithospheric mantle after the breakup of Gondwana) were proposed for basalt at 40°–55°S (e.g., [42,47–49]).

The basalt samples in this study were dredged along the South Mid-Atlantic Ridge between 18.0° and 20.6°S during the China's 26th ocean expedition. Dredge locations are shown in Figure 1, ~800 km west of the Saint Helena Islands and ~1000–1500 km south of the Ascension islands. Most of the basalt samples showed yellowish-brown weathering surface with dark gray fresh surface (Figure 2a–d). Sample preparation and thin section observation were carried out at the Marine Geological Laboratory, School of Marine Sciences, Sun Yat-sen University, Guangzhou, China. The samples are porphyritic rocks (Figures 2a–c and 3a). Phenocrysts represent ~15 vol% of each sample and are composed of mostly plagioclase (>60 vol%, 0.1–0.6 mm), with lesser amounts of olivine (~0.2–0.4 mm) and pyroxene (~0.2–0.5 mm). Phenocrysts exhibit variable grain sizes and are unevenly distributed. Plagioclase shows polysynthetic twinning and occurs in three crystal sizes and morphologies: (1) anhedral to euhedral phenocrysts (~0.1–0.6 mm); (2) anhedral to euhedral microphenocrysts (~0.02–0.06 mm); and (3) lath-shaped to acicular microlites in the matrix (Figure 3a). Olivine and pyroxene phenocrysts occur as euhedral to anhedral grains (Figure 3). The matrix has an intergranular–intersertal texture, and the minerals are mainly plagioclase (>70 vol%), volcanic glass, and small amounts of olivine (<10%) and pyroxene (<10%) (Figure 3).

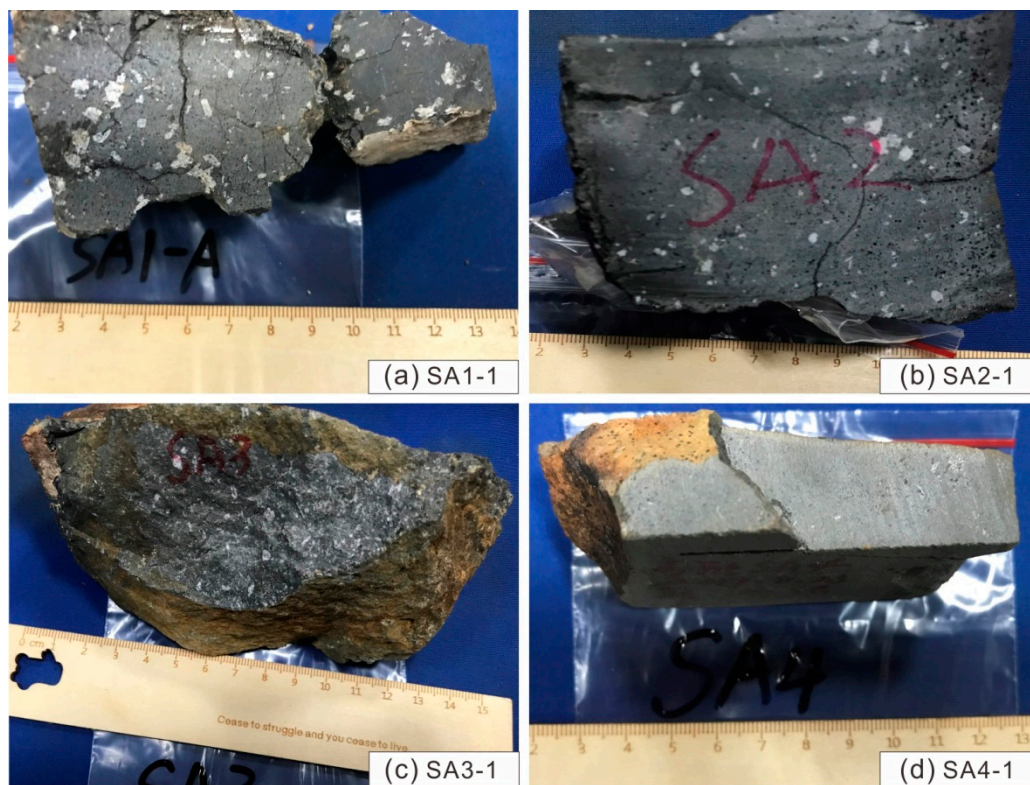


Figure 2. Hand specimen photographs of the South Mid-Atlantic Ridge (SMAR) basalt samples. (a) SA1-1; (b) SA2-1; (c) SA3-1; (d) SA4-1.

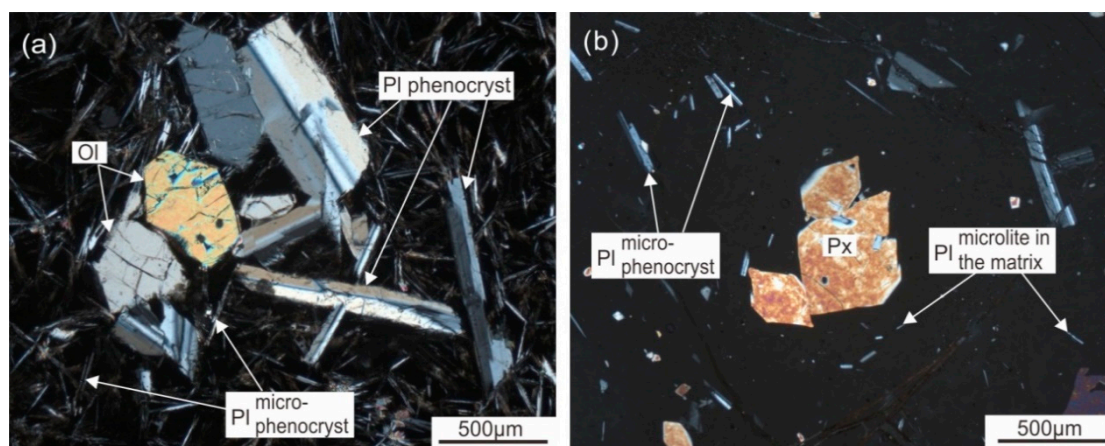


Figure 3. Representative photomicrographs of the SMAR basalt samples. (a) Olivine and plagioclase. Plagioclase generally occurs in three crystal sizes that include phenocryst, microphenocryst, and microlite in the matrix. (b) Pyroxene phenocryst. Ol: olivine; Pl: plagioclase; Px: pyroxene.

3. Analytical Methods

In this paper, twelve basalt samples dredged from four sample locations (Figure 1) were selected for whole-rock major and trace element analyses. Four of these samples were selected for further mineral chemical analyses.

3.1. Whole-Rock Geochemical Analyses

To avoid alteration from seawater, basalt samples were sawed into fresh rock chips (~5 mm in thickness), then they were washed in distilled water, dried and crushed into powers (<200 mesh) using an agate mortar and pestle. Whole-rock major elements were analyzed at the Guangzhou ALS Chemex Company, China following the procedures reported in Chen et al. [50]. A calcined or ignited sample (~0.9 g) was added to ~9.0 g lithium borate flux (50:50 $\text{Li}_2\text{B}_4\text{O}_7$ - LiBO_2), mixed well and fused in an auto fluxer between 1050 °C and 1100 °C. A flat molten glass disk was prepared from the resulting melt. This disk was then analyzed by a PANanalytical Axios X-ray fluorescence spectrometer (XRF) for major elements. Geochemical reference materials (GBW07105/basalt, SARM-4/norite) were used as quality control, and the analytical precision was better than ± 1 –2%.

Whole-rock trace element compositions were analyzed at the Nanjing FocuMS Technology Co. Ltd., China after the procedures reported in Zhong et al. [51]. About 40 mg powder was mixed with 0.5 mL HNO_3 and 1.0 mL HF in high-pressure PTFE bombs. These bombs were steel-jacketed and placed in the oven at 195 °C for 48 h. Rock digestion diluent was nebulized into Agilent Technologies 7700x quadrupole ICP-MS to determine the trace elements. Standard samples, including BHVO-2 (basalt), BCR-2 (basalt), and AGV-2 (andesite), were treated as quality control. Measured values of these reference materials were compared with those of preferred values in GeoReM database [52]. Analytical precisions were better than ± 10 % and ± 5 % for the elements that exceeded 10 ppm and 50 ppm, respectively. Major and trace element data are listed in Table S1.

3.2. Mineral Chemical Analyses

Major element analysis of plagioclase and olivine was conducted using electron probe microanalysis with an EPMA-1720 series electron probe (Shimadzu, Japan) at the National Demonstration Center for Experimental Geology Education, Chengdu University of Technology, Sichuan, China. Mineral compositions were determined using a beam diameter of 10 μm with an acceleration potential of 15 kV and a beam current of 10 nA. Natural minerals and synthetic oxides were used as standards; precisions were better than 1.0%. Backscattered electron (BSE) images were used for image analysis. The analytical data are shown in Table S2.

4. Results

4.1. Whole-Rock Geochemical Compositions

The SMAR basalt samples yielded negative LOI (loss on ignition) values ranging from -0.92 to -0.29 wt% (Table S1). Rapid crystallization of middle ocean ridge basalts in anoxic seafloor environments causes magnetite or pyrrhotite precipitation; during ignition Fe^{2+} will become Fe^{3+} , which increases the apparent weight resulting in a negative LOI value. This may account for the negative LOI values of our samples as negative LOI values are observed in many ocean-floor basalts worldwide (e.g., [51,53]).

Twelve SMAR basalt samples displayed a relatively wide range of whole-rock major element contents (Table S1) with SiO_2 contents ranging from 47.87 to 50.05 wt%, Al_2O_3 from 15.12 to 17.28 wt%, $\text{Fe}_2\text{O}_3\text{T}$ from 9.10 to 13.29 wt%, TiO_2 from 1.12 to 1.71 wt%, MgO from 7.59 to 8.19 wt%, CaO from 11.05 to 12.25 wt%, and P_2O_5 from 0.09 to 0.17 wt%. The Mg-number ($\text{Mg}^\# = \text{molar Mg}/(\text{Mg} + \text{Fe})$) values varied from 57.2 to 67.5. The K_2O and Na_2O contents were 0.05–0.18 wt% and 2.27–2.76 wt%, respectively, with the total alkali element ($\text{K}_2\text{O} + \text{Na}_2\text{O}$) contents ranging from 2.34 to 2.81 wt%. The low total alkali contents, along with petrographical observation, indicate that the samples had undergone little or slight alteration. Concentrations of Cr and Ni ranged from 299 to 385 ppm and 113 to 142 ppm, respectively. All of the basalt samples plot in the basalt field on the SiO_2 versus ($\text{Na}_2\text{O} + \text{K}_2\text{O}$) diagram (Figure 4a) and belong to tholeiitic rocks on the $\text{FeOT}-(\text{K}_2\text{O} + \text{Na}_2\text{O})-\text{MgO}$ triangular diagram (Figure 4b). Combined with the literature data (excluding the Group 2 basalt samples from the SMAR 19° – 20° S presented by Skolotnev et al. [28]), the SMAR basalts exhibit negative correlations of TiO_2 , Na_2O , FeOT , P_2O_5 , V, and Nb with MgO , whereas they display a positive correlation between Cr and MgO (Figure 5).

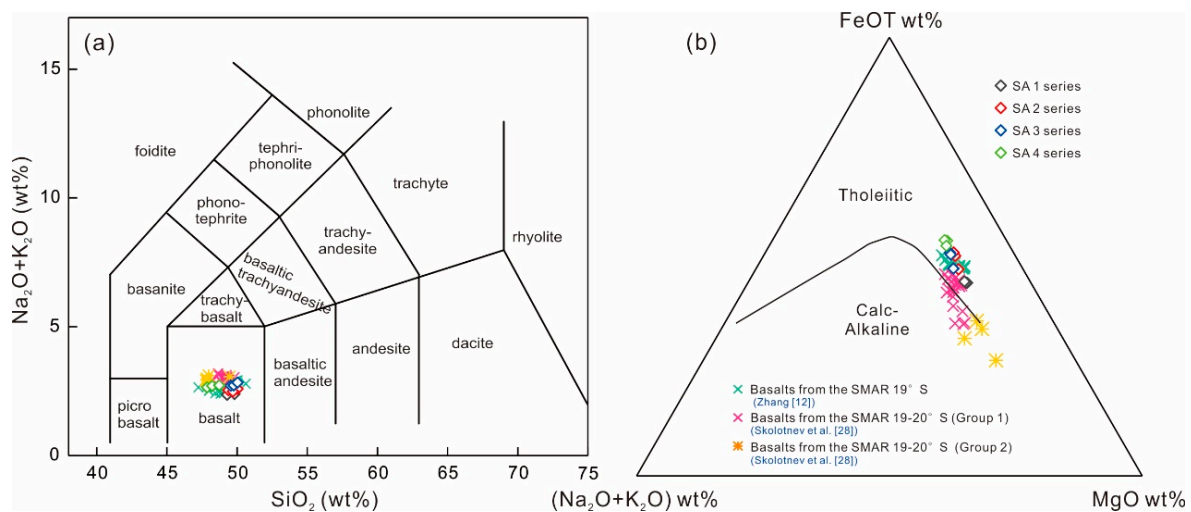


Figure 4. Diagrams of (a) SiO_2 versus ($\text{Na}_2\text{O} + \text{K}_2\text{O}$), as modeled after [54]; and (b) SiO_2 versus $\text{FeOT}-(\text{K}_2\text{O} + \text{Na}_2\text{O})-\text{MgO}$, as modeled after [55], of the SMAR basalt samples. Data for basalts from the SMAR 19° – 20° S are from [12,28].

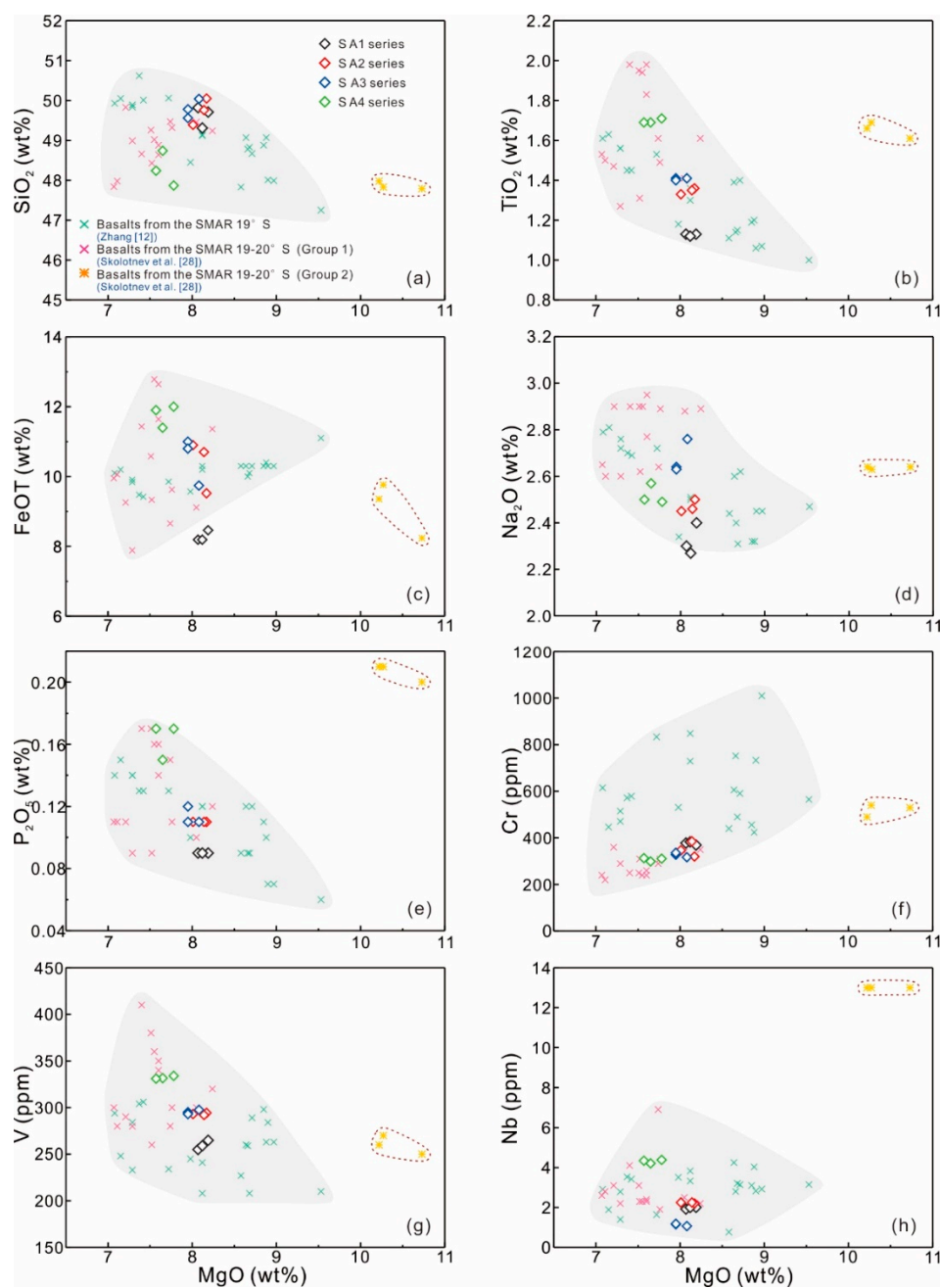


Figure 5. Major and trace element variation diagrams of the SMAR basalt samples from this study and from previous work. Data for basalts from the SMAR 19°–20°S are from [12,28]. Excluding major element SiO₂ (a), the SMAR basalts combined with these basalts from previous study (excluding the Group 2 basalt samples from the SMAR 19°–20°S presented by Skolotnev et al. [28]) exhibit negative correlations of TiO₂, FeOT, Na₂O, P₂O₅, V, and Nb with MgO (b–e,g–h), whereas they display a positive correlation between Cr and MgO (f).

The SMAR basalt samples yielded total rare earth element (REE) concentrations ranging from 37.8 to 61.0 ppm (Table S1), with a mean value of 47.1 ppm. $(La/Yb)_N = 0.54–0.87$, $(La/Sm)_N = 0.47–0.71$, and $(Gd/Yb)_N = 1.11–1.21$ (the subscript N denotes chondrite normalized, normalizing values according to Sun and McDonough [56]). On the chondrite-normalized REE diagram (Figure 6a), these samples exhibit nearly subparallel and N-MORB-like REE patterns and display a slight depletion of light REEs (LREE) compared to heavy REEs (HREE). They had weak negative Eu anomalies (Figure 6a) with δEu ($\delta Eu = Eu_N / (Sm_N \times Gd_N)^{0.5}$) values of 0.86–0.98. On the primitive mantle-normalized multielement

diagram (Figure 6b), all of the basalt samples show N-MORB-like trace element patterns, but some are enriched in Rb, Th, U, and Pb and are depleted in Ba and Sr. Visibly negative Nb–Ta anomalies in SA3 series samples but positive Na–Ta anomalies in SA4 series samples compared to those of N-MORBs were also observed (Figure 6b).

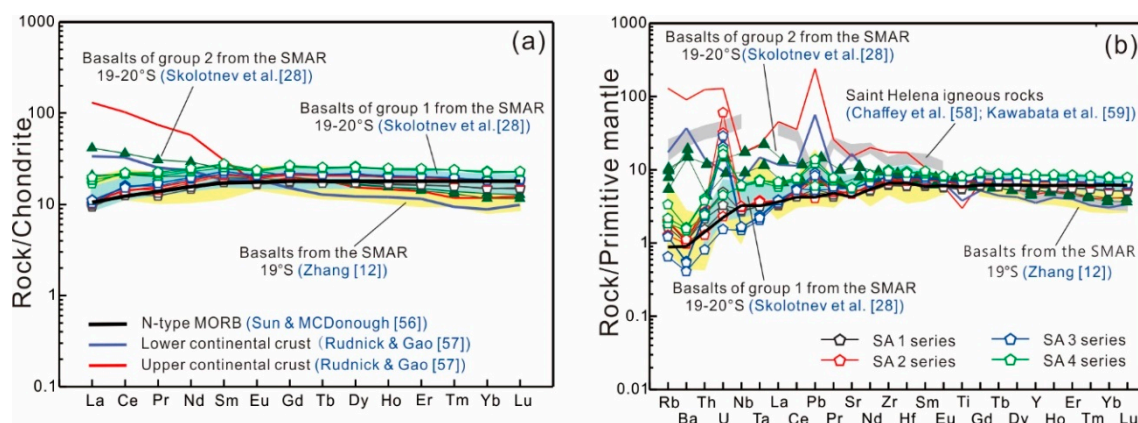


Figure 6. (a) Chondrite-normalized REE and (b) primitive mantle-normalized multielement diagrams of the SMAR basalt samples. The chondrite and primitive mantle normalization and N-type MORB data are from [56]. Upper and lower continental crust data are from [57]. Data for basalts from the SMAR 19°–20°S are from [12,28]. Data for igneous rocks from the Saint Helena islands are from [58,59].

4.2. Mineral Chemical Compositions

The SMAR basalt samples featured porphyritic to intersertal textures and mainly comprised plagioclase with small amounts of olivine and pyroxene (Figure 3). Plagioclase is the most abundant phenocryst, and plagioclase microphenocrysts and microlites in the matrix are also ubiquitous. Samples SA1-1, SA2-1, SA3-1, and SA4-1 were selected for mineral chemical analyses. Major and trace elements in plagioclase and olivine are listed in Tables S2 and S3, respectively.

4.2.1. Plagioclase

Plagioclase phenocrysts of the SMAR basalt samples are weakly zoned to unzoned in backscatter electron images (Figure 7) but do exhibit compositional zoning. Representative plagioclase phenocrysts (Figure 7) were selected for core–rim transects using electron probe microanalysis. The SiO₂, Al₂O₃, CaO, Na₂O, FeO, MgO, and TiO₂ contents for cores of plagioclase phenocrysts were 46.27–50.78 wt%, 31.14–33.90 wt%, 14.46–16.55 wt%, 1.57–2.99 wt%, 0.26–0.57 wt%, 0.07–0.25 wt%, and 0.003–0.100 wt%, respectively (Table S2). Plagioclase rims had SiO₂, Al₂O₃, CaO, Na₂O, FeO, MgO, and TiO₂ concentrations that ranged from 50.23 to 52.86 wt%, 29.83 to 32.20 wt%, 13.25 to 14.51 wt%, 2.77 to 3.61 wt%, 0.38 to 0.82 wt%, 0.13 to 0.31 wt%, and 0.03 to 0.09 wt%, respectively (Table S2). The anorthitic (An) contents for plagioclase phenocrysts were 72–83 for cores and 65–71 for rims (Table S2). In addition, the SiO₂, Al₂O₃, CaO, Na₂O, FeO, MgO, and TiO₂ contents of plagioclase microphenocrysts were 48.63–55.02 wt%, 26.44–31.86 wt%, 11.22–14.56 wt%, 2.88–4.32 wt%, 0.43–2.74 wt%, 0.20–2.46 wt%, and 0.03–0.25 wt%, respectively (Table S2), with An contents ranging from 54 to 72 yielding an average value of 64 (Table S2; Figure 7). Cores of plagioclase phenocrysts had bytownite compositions whereas rims had bytownite to labradorite compositions (Figure 8). Plagioclase microphenocrysts ranged in composition from labradorite to bytownite (Figure 8).

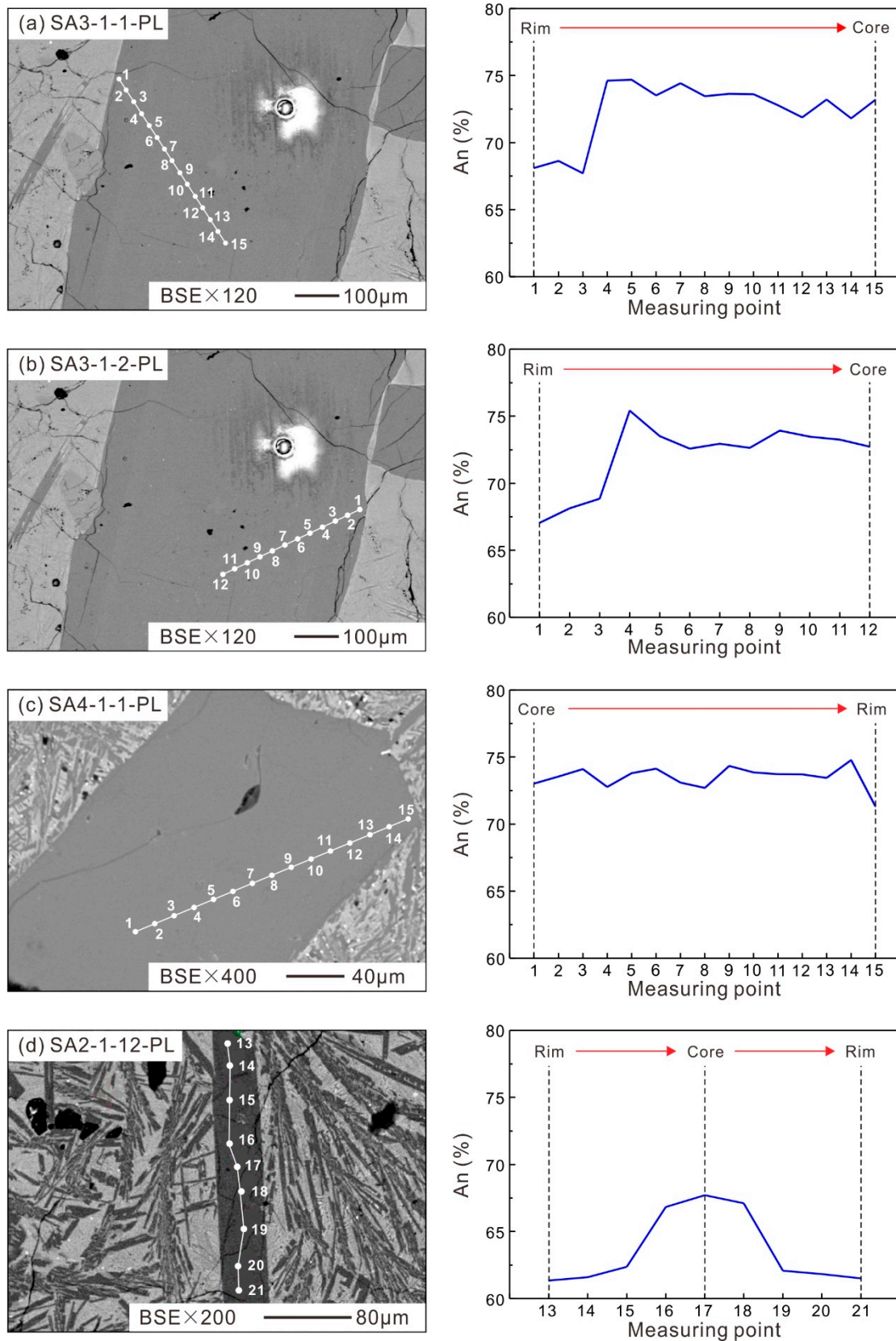


Figure 7. Backscattered electron images of (a–c) plagioclase phenocrysts and (d) a microphenocryst; along with the corresponding variational curves for measured anorthite proportions (mol%).

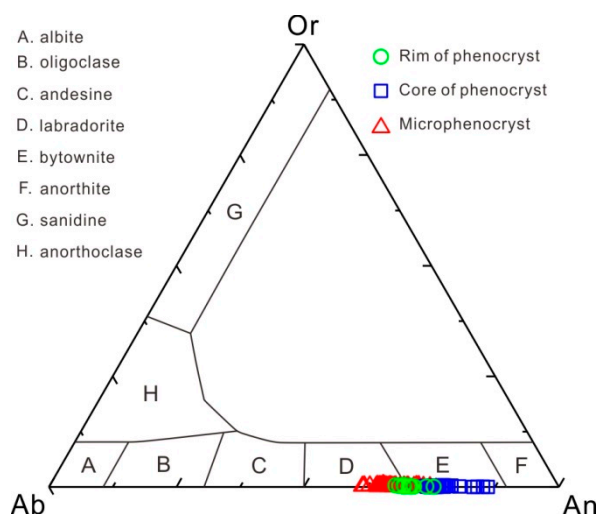


Figure 8. Or–Ab–An classification diagram of plagioclase phenocrysts and microphenocrysts.

4.2.2. Olivine

Olivine phenocrysts in the SMAR basalt samples (SA1-1, 2-1, and 4-1; Figure 9) had variable compositions (Table S3). They had values of Fo87 to Fo96 with an average value of Fo95, suggesting that the primary magmas experienced varying degrees of fractional crystallization. The SiO₂, Al₂O₃, Na₂O, FeO, MgO, and TiO₂ contents were 35.52–40.70 wt%, 0.01–0.52 wt%, 0.003–1.480 wt%, 11.18–28.83 wt%, 32.76–46.52 wt%, and 0.002–0.086 wt%, respectively. The CaO contents ranged from 0.27 to 0.54 wt% and were higher than 0.1 wt%, indicating that olivine phenocrysts were the products of fractional crystallization [60]. The MnO and NiO contents ranged from 0.12 to 0.48 wt% and from 0.01 to 0.29 wt%, respectively. The Fe/Mn ratios ranged from 49 to 124, with an average value of 65 that resembles those of crystalline olivines crystallized from initial melts of the mantle source (60–70 [61]). Concentrations of Cr₂O₃ were low and ranged from 0.01 to 0.15 wt%.

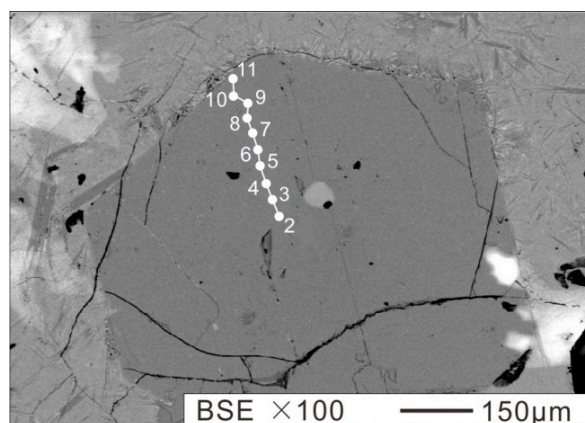


Figure 9. Backscattered electron image for typical olivine phenocryst (SA1-1).

5. Petrogenesis

Basaltic magmas at mid-ocean ridges originate from decompression melting of the upper mantle, but this process can be complex and result in diverse basalt compositions. Previous studies proposed that N-MORBs have low K/Ti ratios of 0.04–0.15 [62] and (La/Sm)_N ratios of less than 0.85 [63]. The SMAR basalt samples investigated here had K/Ti and (La/Sm)_N ratios of 0.05–0.15 and 0.47–0.71, respectively, that, when combined with their N-MORB-like normalized patterns shown in Figure 6, suggest that the SMAR basalt samples belong to the N-MORB group. The compositional diversity observed in MORB can be a result of multiple factors that include: (1) mineralogical and chemical heterogeneities in mantle

sources; (2) variable percentage of melting of the mantle sources; and (3) final magma compositions altered by fractional crystallization and magma replenishment (e.g., [3,10,18,26,30,64]).

5.1. Crystal Fractionation

The compositions of mantle-derived magma can be modified by crystal fractionation prior to emplacement at or near the surface [65]. Generally, MORBs do not appear to be primary magmas produced by partial melting of the mantle but have experienced various degrees of fractional crystallization (e.g., [18,66–72]). Magma chamber and conduit systems are important places for fractional crystallization where mineral–melt separation can occur. Considering the presence of phenocrysts and microphenocrysts in a finer-grained matrix of the SMAR basalts (Figure 3a), they may have experienced two stages of fractional crystallization [73]. In addition, the SMAR basalt samples yielded $Mg^\#$ values ranging from 57.2 to 67.5 with an average value of 62.2 which are lower than those of primary basaltic magmas (68–75) reported by [74]. The concentrations of transition elements such as Ni in the SMAR basalt samples (114–146 ppm) were also quite different from that of typical primary basaltic magmas (300–400 ppm [75]). These compositional signatures as well as the variable plagioclase crystal sizes and compositional variations in olivine phenocrysts indicate that crystal fractionation played an important role in the petrogenesis of the SMAR basalt samples.

Covariation among major and trace elements suggest that fraction of several minerals contributed to the composition of the SMAR basalts. Covariation of Cr and MgO (Figure 5) indicate fractionation of olivine and clinopyroxene whereas the negative correlations of TiO_2 , FeOT, and V with MgO suggest that Fe–Ti oxides fractionation. Negative correlations of Na_2O and P_2O_5 with MgO indicate the accumulation of plagioclase and apatite. There is no linear relationship between MgO and Al_2O_3 (not shown), which is inconsistent magma mixing. Mixing of a primitive magma with a magma that has experienced extensive plagioclase fractionation is expected to result in a mixed magma that inherits a small Eu anomaly [67]. The SMAR basalt samples have slight negative Eu anomalies (Figure 6a) with δEu values ranging from 0.86 to 0.98, which supports this inference.

5.2. Magma Mixing

Fractional crystallization in MORBs probably occurs not in a closed system but in continuously replenished sub-ridge magma chambers [76]. Mixing of primitive and evolved basaltic magma may play a role in the formation of some, if not most, MORBs [77,78]. As discussed above, plagioclase in the SMAR basalt samples occur as phenocrysts, microphenocrysts, and microlites in the matrix (Figure 3a). These features, along with the compositional zoning plagioclase phenocrysts (Figure 7) with reverse zoning of An values from core to rim (Figure 7), suggest that the magmas of the SMAR basalt samples likely have experienced multiple stages of mixing.

Plagioclase compositional zoning records the physical and chemical conditions of magma evolution during crystallization (e.g., [24,79–82]). Magma compositions can change as a function of pressure and temperature (P – T) conditions during plagioclase crystallization [83,84]. Thus, if we can determine the crystallization temperatures of plagioclase, we can investigate the compositional variations in magmas as a function of temperature. Crystallization temperatures of measured plagioclase were calculated using the thermometer given by Putirka [84] with the equation layout:

$$\frac{10^4}{T(K)} = 6.12 + 0.257 \ln \left(\frac{[An^{Pl}]}{[Ca^{liq} (Al^{liq})^2 (Si^{liq})^2]} \right) - 3.166 [Ca^{liq}] + 0.2166 [H_2O^{liq}] - 3.137 \left[\frac{Al^{liq}}{Al^{liq} + Si^{liq}} \right] + 1.216 [Ab^{Pl}]^2 - 2.475 \times 10^{-2} [P(Kbar)] \quad (1)$$

In this equation, T and P are in Kelvin and Kbar, respectively; An^{Pl} and Ab^{Pl} are the fractions of anorthite (An) and albite (Ab) in plagioclase, calculated as cation fractions: $An = CaO / (CaO + NaO_{0.5} + KO_{0.5})$, and $Ab = NaO_{0.5} / (CaO + NaO_{0.5} + KO_{0.5})$. Terms such as Al^{liq} refer to the anhydrous cation

fraction of Al in the liquid; H₂O is in units of wt%. Errors in this model are comparable to those for clinopyroxene thermobarometers: $R = 0.99$ and the standard error of estimate (SEE) is 23 K [84].

Due to the different P – T conditions during crystallization processes, the crystallization temperatures of cores of plagioclase phenocrysts were calculated at P (kbar) = 1 kbar, along with those of rims of plagioclase phenocrysts and plagioclase microphenocrysts at P (kbar) = 0.5 kbar [31]. In this paper, the calculated crystallizing temperatures of cores of plagioclase phenocrysts were ~1180–1240 °C, with an average value of 1200 °C resembling that of the SMAR 18°S basalts (1210 °C) presented by [31]; and those of rims were 1090–1120 °C, with an average value of 1100 °C, also resembling that of the SMAR 18°S basalts (1085 °C) reported by [31] (Table S2). However, the estimated crystallization temperatures of plagioclase microphenocrysts were 980–1060 °C, with an average value of 1023 °C which is lower than that of the SMAR 18°S basalts (1080 °C) given by [31] (Table S2). The estimated crystallization temperatures of compositionally zoned plagioclase phenocrysts are shown in Figure 10.

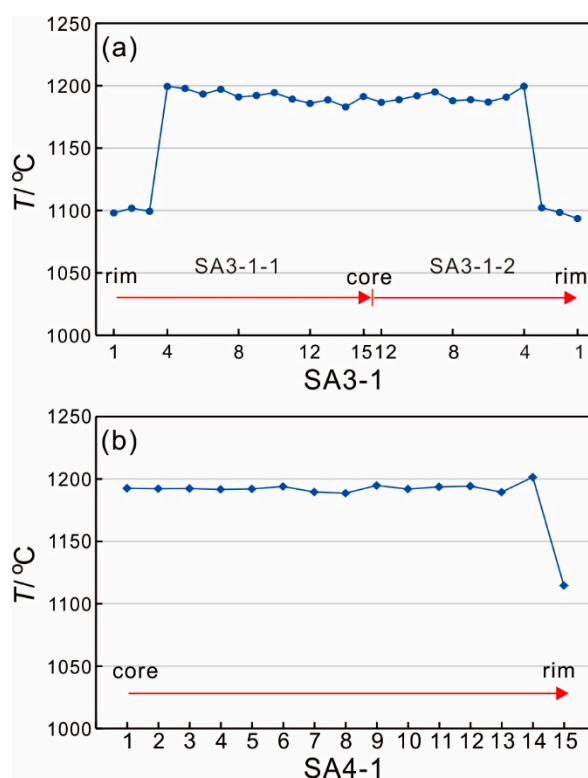


Figure 10. Diagram of the estimated crystallization temperatures of zoned plagioclase phenocrysts. The crystallization temperatures from core to rim decreased sharply for typical plagioclase phenocrysts. (a): sample SA3-1; b): sample SA4-1.

Crystallization temperatures of rims of plagioclase phenocrysts are predicted to be higher than those of plagioclase microphenocrysts, but both of them were lower than those of cores of plagioclase phenocrysts (the temperatures from core to rim decreased sharply by nearly 90–100 °C for typical plagioclase phenocrysts, Figure 10). The crystallization temperatures (1200 °C → 1100 °C, average values) and An contents (74 → 68, average values) from core to rim decreased sharply, which suggests that the physical and chemical conditions for the development of plagioclase in the cores and rims changed as a step function. The relatively high An contents and crystallization temperatures suggest that the cores of plagioclase phenocrysts may be xenocrysts (e.g., [31,83,85]). In addition, the rims of plagioclase phenocrysts exhibited higher An values (68, an average value) and crystallization temperatures (1100 °C, an average value) than those of the plagioclase microphenocrysts (64 and 1023 °C, respectively; average values). Combined with the variable crystal sizes of plagioclase microphenocrysts (Figure 3), these characteristics suggest that the rims of plagioclase phenocrysts and

the plagioclase microphenocrysts may have been generated in different environments such as magma chambers or magma channels, respectively [31].

5.3. Nature of the Magma Sources

Variations in the isotopic compositions and incompatible element ratios in MORB suites have been interpreted to indicate a heterogeneous mantle source (e.g., [34,86,87]). Several types of mantle end-members have been proposed that include DM, EMI (enriched mantle type I), EMII (enriched mantle type II), HIMU, and FOZO (focus zone) (e.g., [4,88–90]). The SMAR basalt samples feature N-MORB-like geochemical compositions, which indicate that they were derived from a DM source. On the Nb/Yb versus Th/Yb diagram (Figure 11a), SMAR samples plot near the N-MORB field that supports a DM source. The La/Sm and Sm/Yb ratios are also compatible with an N-MORB classification and a DM source (Figure 11b).

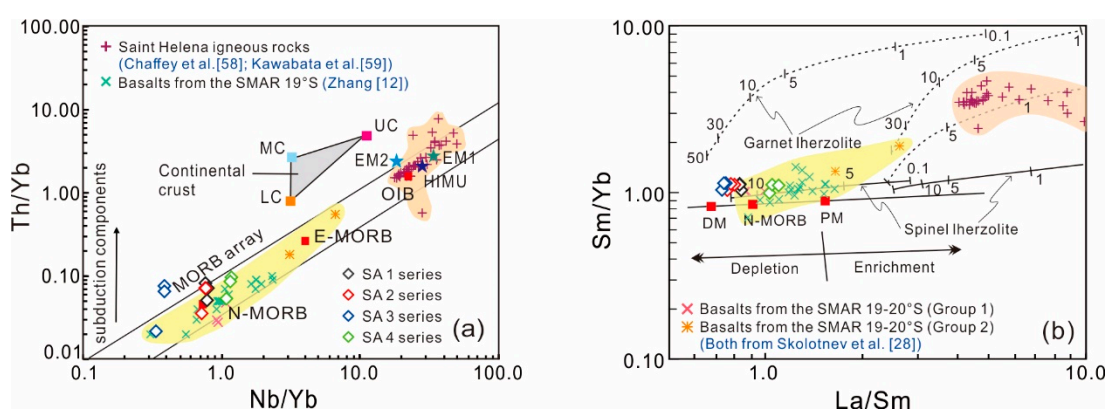


Figure 11. Plots of the SMAR basalt samples: (a) Nb/Yb versus Th/Yb, after [91] and references therein; (b) La/Sm versus Sm/Yb, after [92] and references therein. MORB: mid-ocean ridge basalt; N-MORB: normal mid-ocean ridge basalt; E-MORB: enriched mid-ocean ridge basalt; OIB: ocean island basalt. DM: depleted mantle; PM: primitive mantle; LC: lower crust; UC: upper crust; MC: middle crust. Data for basalts from the SMAR 19°–20°S are from [12,28]. Data for igneous rocks from the Saint Helena islands are from [58,59].

Na_8 and Fe_8 (corrected for crustal level crystallization to 8.0 wt% MgO) are geochemical parameters adopted to assess the extent and pressure (depth) of partial melting of the mantle source; there is a negative correlation of Na_8 values versus melting degrees of mantle source but a positive correlation between Fe_8 values and depths of melting of mantle source (e.g., [7–9,23,93–97]). Previous studies demonstrated that magmas derived from low degrees of partial melting (high Na_8 values) generally originated from a relatively shallow magma source region (low Fe_8 values) [3,7]. However, the SMAR basalt samples (this study and previous work) show a nearly positive correlation between Fe_8 and Na_8 (Figure 12), although the SA2, SA3 and SA4 series show a nearly negative correlation between Fe_8 and Na_8 . All of the basalt samples have relatively high Fe_8 (7.06–9.83) but low Na_8 (2.29–2.77) values revealing that they were likely derived from a deep magma source region with high degrees of partial melting. Overall, the SA1 series samples originated from a relatively shallow magma source region with higher degrees of partial melting relative to the other samples; the SA3 series samples to the south (Figure 1) were produced with relatively lower degrees of partial melting compared to the other samples; and the SA4 series samples were generated with a relatively deeper magma source region relative to the other samples. However, the mineral assemblage in the mantle source changes with depth from plagioclase peridotite at the depth of ~30 km, spinel peridotite at the depth of ~30–80 km, and garnet peridotite at the depths greater than ~80 km (e.g., [98,99]). Generally, REE patterns can be used to determine the potential mineral assemblage during mantle melting and hence approximate the depth of melting [92]. The SMAR basalt samples have low $(\text{Tb}/\text{Yb})_N$ ratios of 1.09–1.18 (<2) that

suggest a spinel-bearing mantle source [100]. Covariation between La/Sm and Sm/Yb ratios suggests a garnet lherzolite source [92]. In the plot of La/Sm versus Sm/Yb (Figure 11b), the SMAR basalt samples have low La/Sm and Sm/Yb values that plot on or near the spinel lherzolite melting curve, thus suggesting that these rocks were probably produced by ~8–22% partial melting of a mantle source composed of spinel lherzolite at moderate depths. Our inference is consistent with the partial melting model that most MORBs are derived from decompression-triggered partial melting at depths of 12–21 kbar (40–65 km) with 10–20% melting [9].

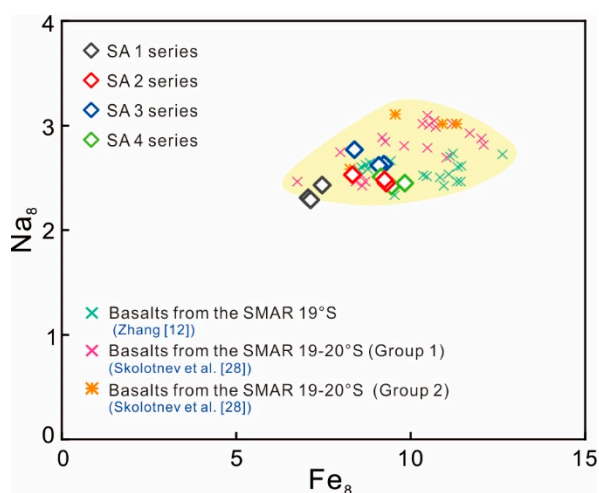


Figure 12. Plots of Fe_8 versus Na_8 of the SMAR basalt bulk rock samples. Data for basalts from the SMAR 19°–20°S are from [12,28].

The SA4 series samples have slightly higher $(La/Sm)_N$ ratios of 0.66–0.71 than that of N-MORBs (0.61 [56]) (Figure 6a). These characteristics, combined with high Th compared to that of N-MORBs (Figure 6b) and some samples with high Th/Yb ratios that plot above the MORB array (Figure 11a), suggest that some SMAR basalt samples contain enriched components. One potential source of an enriched component is subducted sediment. Only four of forty marine sediments determined by Plank and Langmuir [101] yield $(Th/Nb)_{PM}$ (the subscript “PM” represents normalization to primitive mantle values) ratios <2 and the average global subducting sediment has $(Th/Nb)_{PM}$ of 6.5. The SMAR basalt samples have low $(Th/Nb)_{PM}$ ratios of 0.41–1.58, which suggests no involvement of marine sediments. However, minor depletions of Nb–Ta in SA3 series samples compared to those of N-MORBs in Figure 6b may argue for minor contamination by subcontinental lithospheric mantle (SCLM) or continental crust (e.g., [102–105]), but this is unlikely given the large distance to the nearest exposure of continental crust. In addition, the primitive mantle-normalized patterns of the SMAR basalt samples are different than those of continental crust [57] (Figure 6b). For example, continental crust has very high Ba and low Ti concentrations that are inconsistent with those of the SMAR basalt samples (Figure 6b). In contrast, the SA4 series samples have relatively high Nb–Ta compared to those of N-MORBs (Figure 6b), indicating a possible contribution from a mantle plume.

Many studies have shown that mantle plume–ridge interaction occurred at the SMAR 3°S to 46°S and this played a role in the production of basalts in this area (e.g., [13,26,28]). Our samples are from near the Saint Helena plume (Figure 1) and previous work suggests that the Saint Helena Islands sample a HIMU source (Saint Helena plume, Figure 6b) (e.g., [58,106–109]). There is an inclined conduit (or low-spreading zone) in the upper mantle that extends from the Saint Helena plume region to the adjacent SMAR zone; this represents a conduit from the plume to the spreading axis [46,110]. Data on the isotopic composition of basalts from the MAR 14°–17°S and 19°–20°S segments suggest that these rocks were probably derived from a mantle substrate contaminated with materials of the Saint Helena plume [28,32], especially the Group 2 enriched basalts whose DM sources contaminated with components enriched in lithophile elements (e.g., Nb, Ta) and Th [28] (Figures 5 and 6b). Considering

that the basalts of the SMAR 18°–20°S, including the samples in this study, show a clearly geochemical trend towards the Saint Helena igneous rocks in Figure 11, we propose that the SA4 series samples—that show high Th, Nb, and Ta relative to those of N-MORB (Figure 6b)—may have been produced in a similar setting. In addition, the Saint Helena primary magmas may originate from partial melting of a depleted peridotitic source with the addition of a small amount of melt derived from recycled ancient subducted oceanic crust [59]. Thus, the possibly involved SCLM component in the formation of the SA3 series samples (with negative Nb–Ta anomalies relative to those of N-MORB in Figure 6b) may have been external to plumes and dispersed into the asthenosphere where it was then sampled by MORB-related magmatism (e.g., [48,111,112]). Although the inclusion of SCLM is speculative, it is clear that the variations in incompatible elements in the SMAR basalt samples indicate a heterogeneous mantle source with depleted and enriched components.

6. Conclusion

Basalts dredged from the South Mid-Atlantic Ridge 18.0°–20.6°S are normal mid-ocean ridge basalt with tholeiitic affinities. Plagioclase occurs as phenocrysts, microphenocrysts, and microlite in the matrix. Plagioclase phenocrysts and microphenocrysts vary from bytownite to labradorite in composition, and olivine phenocrysts are forsterite. The basalts underwent fractional crystallization and possibly magma mixing. Variable crystal sizes, anorthite values, and crystallizing temperatures estimated for plagioclase suggest that cores may be xenocrystic, whereas phenocryst rims and microphenocrysts may be generated in different environments such as magma chambers or magma channels, respectively. The major and trace element compositions of the basalts suggest derivation from a depleted mantle source composed of spinel lherzolite with the involvement of small amounts of enriched components possibly derived from the Saint Helena plume and subcontinental lithospheric mantle in the asthenosphere. The characteristics of the magma sources of the basalts indicate mantle heterogeneity below the South Mid-Atlantic Ridge.

Supplementary Materials: The following are available online at <http://www.mdpi.com/2075-163X/9/11/659/s1>. Table S1: Whole-rock major element (wt%) and trace element (ppm) compositions of the SMAR basalt samples. Table S2: Electron probe microanalytical data of typical plagioclases in the SMAR basalt samples. Table S3: Electron probe microanalytical data of typical olivines in the SMAR basalt samples.

Author Contributions: Conceptualization, W.L.(Weiliang Liu) and Y.Z.; Methodology, W.L.(Weiliang Liu) and Y.Z.; Software, Y.M.; Validation, W.L.(Weiliang Liu) and Y.Z.; Formal Analysis, K.R.; Investigation, Z.S.; Resources, Z.S.; Data Curation, K.R.; Writing—Original Draft Preparation, Y.Z.; Writing—Review & Editing, W.L.(Weiliang Liu) and C.Y.; Visualization, J.L. and W.L.(Wei Li); Supervision, W.L.(Weiliang Liu); Project Administration, B.X.; Funding Acquisition, W.L.(Weiliang Liu).

Funding: This work was supported by the National Nature Science Foundation of China [grants 41972049, 41472054, 41977231, 41502277, 91858208, 41606086], Guangzhou Science Technology and Innovation Commission Project [grant 201904010138], research grant of State Key Laboratory of Isotope Geochemistry, Guangzhou Institute of Geochemistry, Chinese Academy of Sciences [grant SKLaBIG-KF-18-11]; China State Scholarship Fund of visiting scholar [grant 20170638507]; the Special Fund for Basic Scientific Research of Central Colleges, Chang'an University [grants 300102268502, 300102269504]; the Fund of Key Laboratory of Mine Geological Hazards Mechanism and Control [grant 2017KF06]; research grant of State Key Laboratory of Isotope Geochemistry, Guangzhou Institute of Geochemistry, Chinese Academy of Sciences [grant number SKLaBIG-KF-18-11]; National Higher Education Quality Monitoring Data Center of Sun Yat-sen University [grant number G1914] and SYSU Course Construction Project for Postgraduates [grant 201922].

Acknowledgments: We thank teamwork of crews on the China's 26th ocean expedition and marine geologic survey training supported by the South China Sea cruises, South China Sea Institute, SYSU. We are deeply grateful to Lihui Chen, Jianghai Wang, Jianxin Cai, Lifeng Zhong, Wenhuan Chen, Hao Zheng for helpful discussions; Liang Li, Botao Cheng and Xiao Zhang for analytical assistance. We appreciate two anonymous reviewers for their constructive comments and suggestions.

Conflicts of Interest: The authors declare no conflict of interest.

References

1. Wilkinson, J.F.G. The genesis of Mid-ocean ridge basalt. *Earth-Sci. Rev.* **1982**, *18*, 1–57. [[CrossRef](#)]
2. Hart, S.R. A large-scale isotope anomaly in the Southern Hemisphere mantle. *Nature* **1984**, *309*, 753–757. [[CrossRef](#)]
3. Langmuir, C.H.; Klein, E.M.; Plank, T. Petrological systematics of Mid-ocean ridge basalts: Constraints on melt generation beneath ocean ridges. In *Mantle Flow and Melt Generation at Mid-Ocean Ridges*; Blackman, D., Ed.; Wiley: New York, NY, USA, 1992; pp. 183–280.
4. Hoffmann, A.W. Mantle geochemistry: the message from oceanic volcanism. *Nature* **1997**, *385*, 219–228. [[CrossRef](#)]
5. Niu, Y.L.; Batiza, R. Extreme mantle source heterogeneities beneath the Northern East Pacific rise: Trace element evidence from Near-ridge seamounts. In *Proceedings of the 30th International Geological Congress*, Beijing, China, 4–14 August 1996; pp. 109–120.
6. Langmuir, C.H.; Forsyth, D.W. Mantle melting beneath mid-ocean ridges. *Oceanography* **2007**, *20*, 78–89. [[CrossRef](#)]
7. Klein, E.M.; Langmuir, C.H. Global correlations of ocean ridge basalt chemistry with axial depth and crustal thickness. *J. Geophys. Res.-Solid Earth* **1987**, *92*, 8089–8115. [[CrossRef](#)]
8. Niu, Y.L.; Batiza, R. An empirical method for calculating melt compositions produced beneath mid-ocean ridges: Application for axis and off-axis (seamounts) melting. *J. Geophys. Res.* **1991**, *96*, 21753–21777. [[CrossRef](#)]
9. Niu, Y.; Hékinian, R. Spreading-rate dependence of the extent of mantle melting beneath ocean ridges. *Nature* **1997**, *385*, 326–329. [[CrossRef](#)]
10. Rubin, K.H.; Sinton, J.M. Inferences on mid-ocean ridge thermal and magmatic structure from MORB compositions. *Earth Planet. Sci. Lett.* **2007**, *260*, 257–276. [[CrossRef](#)]
11. Yu, M. Petrology and Geochemistry Differences of MORB and Their Significance between Fast and Slow Spreading Ridge. Ph.D. Thesis, China University of Geoscience, Beijing, China, 2013.
12. Zhang, H.T. Mid-Oceanic Ridge Basalts (MORBs) Chemistry and Characteristics of Plagioclase-Hosted Melt Inclusions in the South Atlantic Ridge 19°S and Implications for Magmatic Processes. Master's Thesis, First Institute of Oceanography SOA, Qingdao, China, 2015.
13. Qi, Q. Petrogeochemical Characteristics Comparison and Implication for Magmatic Processes of the MORBs between SAR and SWIR. Master's Thesis, Ocean University of China, Qingdao, China, 2015.
14. Kent, G.M.; Harding, A.J.; Orcutt, J.A. Evidence for a smaller magma chamber beneath the East Pacific Rise at 9°30'N. *Nature* **1990**, *344*, 650–653. [[CrossRef](#)]
15. Sinha, M.C.; Constable, S.C.; Peirce, C.; White, A.; Heinson, G.; MacGregor, L.M.; Navin, D.A. Magmatic processes at slow spreading ridges: Implications of the RAMESSES experiment at 57° 45'N on the Mid-Atlantic Ridge. *J. Geophys. J. Int.* **1998**, *135*, 731–745. [[CrossRef](#)]
16. Niu, Y.; Regelous, M.; Wendt, I.J.; Batiza, R.; O'Hara, M.J. Geochemistry of near-EPR seamounts: Importance of source vs. process and the origin of enriched mantle component. *Earth Planet. Sci. Lett.* **2002**, *199*, 327–345. [[CrossRef](#)]
17. Nishio, Y.; Shun'ichi, N.; Ishii, T.; Sano, Y. Isotope systematics of Li, Sr, Nd, and volatiles in Indian Ocean MORBs of the Rodrigues Triple Junction: Constraints on the origin of the DUPAL anomaly. *Geochim. Cosmochim. Acta* **2007**, *71*, 745–759. [[CrossRef](#)]
18. Sinton, J.M.; Detrick, R.S. Mid-Ocean Ridge Magma Chambers. *J. Geophys. Res.* **1992**, *97*, 197–216. [[CrossRef](#)]
19. Scheirer, D.S.; Macdonald, K.C. Variation in cross-sectional area of the axial ridge along the East Pacific Rise: Evidence for the magmatic budget of a fast spreading center. *J. Geophys. Res.-Solid Earth.* **1993**, *98*, 7871–7885. [[CrossRef](#)]
20. Dick, H.J.; Lin, J.; Schouten, H. An ultraslow-spreading class of ocean ridge. *Nature* **2003**, *426*, 405–412. [[CrossRef](#)] [[PubMed](#)]
21. Baker, E.T. Hydrothermal venting in magma deserts: The ultraslow-spreading Gakkel and Southwest Indian Ridges. *Geochem. Geophys. Geosyst.* **2004**, *5*, Q08002. [[CrossRef](#)]
22. Cannat, M.; Sauter, D.; Bezos, A.; Meyzen, C.; Humeler, E.; Rigoleur, M.L. Spreading rate, spreading obliquity, and melt supply at the ultraslow spreading Southwest Indian Ridge. *Geochem. Geophys. Geosyst.* **2008**, *9*, 1525–2027. [[CrossRef](#)]

23. Niu, Y.L.; O'Hara, M.J. Global correlations of ocean ridge basalt chemistry with axial depth: A new perspective. *J. Petrol.* **2008**, *49*, 633–664. [[CrossRef](#)]
24. Zhang, G.L. Characteristics and Implications for Magmatism of the MORBs in the East Pacific Rise 13°N. Ph.D. Thesis, Institute of Oceanology, Chinese Academy of Sciences, Qingdao, China, 2010.
25. Stakes, D.S.; Shervais, J.W.; Hopson, C.A. The volcanic-tectonic cycle of the FAMOUS and AMAR Valleys, Mid-Atlantic Ridge (36°47'N): Evidence from basalt glass and phenocryst compositional variations for a steady state magma chamber beneath the valley midsections, AMAR 3. *J. Geophys. Res.-Solid Earth.* **1984**, *89*, 6995–7028. [[CrossRef](#)]
26. Fontignie, D.; Schilling, J.G. Mantle heterogeneities beneath the South Atlantic: A Nd-Sr-Pb isotope study along the Mid-Atlantic Ridge (3°S–46°S). *Earth Planet. Sci. Lett.* **1996**, *142*, 209–221. [[CrossRef](#)]
27. Escrig, S.; Schiano, P.; Schilling, J.G.; Allegre, C. Rhenium–osmium isotope systematics in MORB from the Southern Mid-Atlantic Ridge (40–50°S). *Earth Planet. Sci. Lett.* **2005**, *235*, 528–548. [[CrossRef](#)]
28. Skolotnev, S.G.; Peive, A.A.; Belyatskii, B.V. Geochemical and isotopic features of basalts in the axial Mid-Atlantic Ridge near the Martin Vaz Fracture Zone, South Atlantic (19°–20° S). *Dokl. Earth Sci.* **2006**, *407*, 401–407. [[CrossRef](#)]
29. Ding, X.; Li, J.; Zheng, C.Q.; Huang, W.; Cui, N.Y.; Dou, Y.G.; Sun, Z.L. Chemical composition of the basalts on East Pacific rise (1.5°N–1.5°S) and South Mid-Atlantic ridge (13.2°S). *Marin. Geol. Quat. Geol.* **2014**, *34*, 57–66.
30. Turner, S.; Kokfelt, T.; Hauff, F.; Hasse, K.; Lundstrom, C.; Hoernle, K.; Yeo, I.; Devey, C. Mid-ocean ridge basalt generation along the slow-spreading, South Mid-Atlantic Ridge (5–11°S): Inferences from ²³⁸U–²³⁰Th–²²⁶Ra disequilibria. *Geochim. Cosmochim. Acta* **2015**, *169*, 152–166. [[CrossRef](#)]
31. Qi, Q.; Lai, Z.Q.; Long, X.J.; Leng, C.X.; Zhao, G.T. Characteristics and Petrogenesis Significance of Plagioclases in Basalt from the South Mid-Atlantic Ridge. *Perio. China Univ. Ocean.* **2016**, *46*, 105–112, (In Chinese with English Abstract).
32. Hargraves, R.B. Faster spreading or greater ridge length in the Archean? *Geology* **1986**, *14*, 50–752. [[CrossRef](#)]
33. Hanan, B.B.; Kingsley, R.H.; Schilling, J. Pb isotope evidence in the South Atlantic for migrating ridge—hotspot interactions. *Nature* **1986**, *322*, 137–144. [[CrossRef](#)]
34. Schilling, J.G.; Zajac, M.; Evans, R.; Johnston, T.; White, W.; Devine, J.D.; Kingsley, R. Petrologic and geochemical variations along the Mid-Atlantic Ridge from 29 degrees N to 73 degrees N. *Am. J. Sci.* **1983**, *283*, 510–586. [[CrossRef](#)]
35. Blichert-Toft, J.; Agraniér, A.; Andres, M.; Kingsley, R.; Schilling, J.G.; Albarede, F. Geochemical segmentation of the Mid-Atlantic Ridge north of Iceland and ridge–hot spot interaction in the North Atlantic. *Geochim. Geophys. Geosyst.* **2005**, *6*, 1525–2027. [[CrossRef](#)]
36. Beltenev, V.E.; Skolotnev, S.G.; Rozhdestvenskaya, I.I. New chemical and isotopic data for basalts from the axial segment of the Mid-Atlantic ridge between the Vema and Mercury fracture zones. *Dokl. Earth Sci.* **2014**, *459*, 1488–1494. [[CrossRef](#)]
37. Smith, W.H.F.; Sandwell, D.T. Global seafloor topography from satellite altimetry and ship depth soundings. *Science* **1997**, *277*, 1957–1962. [[CrossRef](#)]
38. Larson, R.L.; Ladd, J.W. Evidence for the Opening of the South Atlantic in the Early Cretaceous. *Nature* **1973**, *246*, 209–212. [[CrossRef](#)]
39. Torsvik, T.H.; Rouse, S.; Labails, C.; Smethurst, M.A. A new scheme for the opening of the South Atlantic Ocean and the dissection of an Aptian salt basin. *Geophys. J. Int.* **2009**, *177*, 1315–1333. [[CrossRef](#)]
40. Valencio, D.A.; Mendiá, J.E.; Giudici, A.; Gascon, J.O. Palaeomagnetism of the Cretaceous Pirgua Subgroup (Argentina) and the age of the opening of the South Atlantic. *Geophys. J. Int.* **2007**, *51*, 47–58. [[CrossRef](#)]
41. Storey, B.C. The role of mantle plumes in continental breakup: case histories from Gondwanaland. *Nature* **1995**, *377*, 301–308. [[CrossRef](#)]
42. le Roux, P.J.; Roex, A.L.; Schilling, J.G. Crystallization processes beneath the southern Mid-Atlantic Ridge (40–55°S), evidence for high-pressure initiation of crystallization. *Contrib. Mineral. Petrol.* **2002**, *142*, 582–602. [[CrossRef](#)]
43. Hawkesworth, C.J.; Gallagher, K.; Kelley, S.; Mantovani, M.; Peate, D.W.; Regelous, M.; Rogers, N.W. Parana magmatism and the opening of the South Atlantic. *Geol. Soc. Lond. Spec. Publ.* **1992**, *68*, 221–240. [[CrossRef](#)]
44. Wilson, M. Magmatism and continental rifting during the opening of the South Atlantic Ocean: a consequence of Lower Cretaceous super-plume activity? *Geol. Soc. Lond. Spec. Publ.* **1992**, *68*, 241–255. [[CrossRef](#)]

45. Shi, X.F.; Li, B.; Ye, J.; Li, C.X. Hydrothermal activity and formation mechanism of the South Atlantic Mid-ridge. *J. Min.* **2015**, *S1*, 782–783. (In Chinese)
46. Zhang, Y.S.; Tanimoto, T.; Stolper, E.M. S-wave velocity, basalt chemistry and bathymetry along the Mid-Atlantic Ridge. *Phys. Earth Planet. Inter.* **1994**, *79*, 0–93. [[CrossRef](#)]
47. Douglass, J.; Schilling, J.G. Systematics of three-component, pseudo-binary mixing lines in 2D isotope ratio space representations and implications for mantle plume–ridge interaction. *Chem. Geol.* **2000**, *163*, 1–23. [[CrossRef](#)]
48. Douglass, J.; Schilling, J.G.; Fontignie, D. Plume-ridge interactions of the Discovery and Shona mantle plumes with the southern Mid-Atlantic Ridge (40°–55°S). *J. Geophys. Res.-Solid Earth.* **1999**, *104*, 2941–2962. [[CrossRef](#)]
49. Kamenetsky, V.S.; Maas, R.; Sushchevskaya, N.M.; Norman, M.D.; Cartwright, I.; Peyve, A.A. Remnants of Gondwanan continental lithosphere in oceanic upper mantle: Evidence from the South Atlantic Ridge. *Geology* **2001**, *29*, 243–246. [[CrossRef](#)]
50. Chen, L.; Zhao, Z.F.; Zheng, Y.F. Origin of andesitic rocks: Geochemical constraints from Mesozoic volcanics in the Luzong basin, South China. *Lithos* **2014**, *190*, 220–239. [[CrossRef](#)]
51. Zhong, Y.; Chen, L.H.; Wang, X.J.; Zhang, G.L.; Xie, L.W.; Zeng, G. Magnesium isotopic variation of oceanic island basalts generated by partial melting and crustal recycling. *Earth Planet. Sci. Lett.* **2017**, *463*, 127–135. [[CrossRef](#)]
52. Jochum, K.P.; Nohl, U. Reference materials in geochemistry and environmental research and the GeoReM database. *Chem. Geol.* **2008**, *253*, 50–53. [[CrossRef](#)]
53. Li, W.; Tao, C.; Zhang, W.; Liu, J.; Liang, J.; Liao, S.; Yang, W. Melt Inclusions in Plagioclase Macrocysts at Mount Jourdanne, Southwest Indian Ridge (~64°E): Implications for an Enriched Mantle Source and Shallow Magmatic Processes. *Minerals* **2019**, *9*, 493. [[CrossRef](#)]
54. Le BAS, M.J.; Maitre, R.W.L.E.; Streckeisen, A.; Zanettin, B. A chemical classification of volcanic rocks based on the total alkali-silica diagram. *J. Petrol.* **1986**, *27*, 745–750. [[CrossRef](#)]
55. Irvine, T.N.J.; Baragar, W.R.A. A guide to the chemical classification of the common volcanic rocks. *Can. J. Earth Sci.* **1971**, *8*, 523–548. [[CrossRef](#)]
56. Sun, S.S.; McDonough, W.F. Chemical and isotopic systematics of oceanic basalt: Implication for mantle composition and processes. *Spec. Publ. Geol. Soc. London.* **1989**, *42*, 313–345. [[CrossRef](#)]
57. Rudnick, R.; Gao, S. The role of lower crustal recycling in continent formation. *Geochim. Cosmochim. Acta.* **2003**, *67*, 1–10.
58. Chaffey, D.J.; Cliff, R.A.; Wilson, B.M. Characterization of the St Helena magma source. *Geo. Soc. Lond. Spec. Publ.* **1989**, *42*, 257–276. [[CrossRef](#)]
59. Kawabata, H.; Hanyu, T.; Chang, Q.; Kimura, J.I.; Nichols, A.R.L.; Tatsumi, Y. The petrology and geochemistry of St. Helena alkali basalts: evaluation of the oceanic crust-recycling model for HIMU OIB. *J. Petrol.* **2011**, *52*, 791–838. [[CrossRef](#)]
60. Ren, Z.Y.; Takahashi, E.; Orihashi, Y.; Johnson, K.T.M. Petrogenesis of tholeiitic lavas from the submarine Hana Ridge, Haleakala volcano, Hawaii. *J. Petrol.* **2004**, *45*, 2067–2099. [[CrossRef](#)]
61. Herzberg, C. Identification of source lithology in the Hawaiian and Canary Islands: Implications for origins. *J. Petrol.* **2011**, *52*, 113–146. [[CrossRef](#)]
62. Tarney, J.; Wood, D.A.; Saunders, A.D.; Cann, J.R.; Varet, J. Nature of Mantle Heterogeneity in the North Atlantic: Evidence from Deep Sea Drilling. *Philos. Trans. R. Soc. B-Biol. Sci.* **1980**, *297*, 179–202. [[CrossRef](#)]
63. Xu, X.S.; Qiu, J.S. *Igneous Petrology*; Science Press: Beijing, China, 2010; pp. 183–184.
64. Couch, S.; Sparks, R.S.J.; Carroll, M.R. Mineral disequilibrium in lavas explained by convective self-mixing in open magma chambers. *Nature* **2001**, *411*, 1037–1039. [[CrossRef](#)]
65. Wittke, J.H.; Mack, L.E. OIB-Like Mantle Source for Continental Alkaline Rocks of the Balcones Province, Texas: Trace-Element and Isotopic Evidence. *J. Geol.* **1993**, *101*, 333–344. [[CrossRef](#)]
66. Bryan, W.B. Regional variation and petrogenesis of basalt glasses from the FAMOUS area, Mid-Atlantic Ridge. *J. Petrol.* **1979**, *20*, 293–325. [[CrossRef](#)]
67. Roex, A.P.L.; Erlank, A.J.; Needham, H.D. Geochemical and mineralogical evidence for the occurrence of at least three distinct magma types in the ‘famous’ region. *Contrib. Mineral. Petrol.* **1981**, *77*, 24–37. [[CrossRef](#)]
68. Danyushevsky, L.V. The effect of small amounts of H₂O on crystallisation of mid-ocean ridge and backarc basin magmas. *J. Volcanol. Geotherm. Res.* **2001**, *110*, 265–280. [[CrossRef](#)]

69. Coogan, L.A.; Jenkin, G.R.; Wilson, R.N. Constraining the cooling rate of the lower oceanic crust: a new approach applied to Oman ophiolite. *Earth Planet. Sci. Lett.* **2002**, *199*, 127–146. [[CrossRef](#)]
70. O'Hara, M.J.; Herzberg, C. Interpretation of trace element and isotope features of basalts: relevance of field relations, petrology, major element data, phase equilibria, and magma chamber modeling in basalt petrogenesis. *Geochim. Cosmochim. Acta* **2002**, *66*, 2167–2191. [[CrossRef](#)]
71. Zhang, G.L.; Zeng, Z.G.; Yin, X.B.; Chen, D.G.; Wang, X.Y.; Wang, X.M. Periodical mixing of MORB magmas near East Pacific Rise 13 N: evidence from modeling and zoned plagioclase phenocrysts. *J. Geophys. Res.-Solid Earth.* **2008**, *51*, 1786. [[CrossRef](#)]
72. Miao, Y.U.; Xin, S.U.; Tao, C.H.; Wu, G.H.; Li, H.M.; Lou, H.L. Petrological and Geochemical Features of Basalts at 49.6°E and 50.5°E Hydrothermal Fields along the Southwest Indian Ridge. *Geoscience* **2013**, *3*. (In Chinese with English Abstract).
73. Gill, R. *Igneous Rocks and Processes: A Practical Guide*; Wiley-Blackwell: West Sussex, UK, 2010.
74. Green, D.H. Experimental testing of "equilibrium" partial melting of peridotite under water-saturated, high-pressure conditions. *Can. Mineral.* **1976**, *14*, 255–268.
75. Frey, F.A.; Green, D.H.; Roy, S.D. Integrated models of basalt petrogenesis: A study of quartz tholeiites to olivine melilitites from southeastern Australia utilizing geochemical and experimental petrological data. *J. Petrol.* **1978**, *19*, 463–513. [[CrossRef](#)]
76. O'hara, M.J. Geochemical evolution during fractional crystallisation of a periodically refilled magma chamber. *Nature* **1977**, *266*, 503–507. [[CrossRef](#)]
77. Rhodes, J.M.; Dungan, M.A.; Blanchard, D.P.; Long, P.E. Magma mixing at mid-ocean ridges: Evidence from basalts drilled near 22°N on the Mid-Atlantic Ridge. *Tectonophysics* **1979**, *55*, 35–61. [[CrossRef](#)]
78. Walker, D.; Shibata, T.; DeLong, S.E. Abyssal tholeiites from the Oceanographer fracture zone. *Contrib. Mineral. Petrol.* **1979**, *70*, 111–125. [[CrossRef](#)]
79. Nixon, G.T.; Pearce, T.H. Laser-interferometry study of oscillatory zoning in plagioclase; the record of magma mixing and phenocryst recycling in calc-alkaline magma chambers, Iztaccihuatl Volcano, Mexico. *Am. Miner.* **1987**, *72*, 1144–1162.
80. Li, W.X.; Dong, C.W.; Zhou, X.M. Plagioclase xenocryst and magma mingling in Pingtan and Zhangzhou Complexes. *Acta Petrol. Sin.* **1999**, *15*, 586–590, (In Chinese with English Abstract).
81. Perugini, D.; Poli, G.; Valentini, L. Strange attractors in plagioclase oscillatory zoning: Petrological implications. *Contrib. Mineral. Petrol.* **2005**, *149*, 482–497. [[CrossRef](#)]
82. Landi, P.; Métrich, N.; Bertagnini, A.; Rosi, M. Dynamics of magma mixing and degassing recorded in plagioclase at Stromboli (Aeolian Archipelago, Italy). *Contrib. Mineral. Petrol.* **2004**, *147*, 629–631. [[CrossRef](#)]
83. Zhang, R.Y.; Cong, B.L. *Geothermometers and Geobarometers*; Geological Publishing House: Beijing, China, 1983; pp. 142–144.
84. Putirka, K.D. Igneous thermometers and barometers based on plagioclase + liquid equilibria: Tests of some existing models and new calibrations. *Am. Miner.* **2005**, *90*, 336–346. [[CrossRef](#)]
85. Cashman, K.V. Groundmass crystallization of Mount St. Helens Dacite. *Contrib. Mineral. Petrol.* **1980**, *109*, 431–449. [[CrossRef](#)]
86. Wood, D.A.; Joron, J.L.; Treuil, M.; Norry, M.; Tarney, J. Elemental and Sr isotope variations in basic lavas from Iceland and the surrounding ocean floor. *Contrib. Mineral. Petrol.* **1979**, *70*, 319–339. [[CrossRef](#)]
87. Sun, S.S.; Nesbit, R.W.; Sharaskin, A. Chemical characteristics of mid-ocean ridge basalts. *Earth Planet. Sci. Lett.* **1979**, *45*, 119–138. [[CrossRef](#)]
88. White, W.M.; Hofmann, A.W. Mantle heterogeneity and isotopes in oceanic basalts. *Nature* **1982**, *295*, 363–364. [[CrossRef](#)]
89. Zindler, A.; Hart, S. Chemical Geodynamics. *Annu. Rev. Earth Planet. Sci.* **2003**, *14*, 493–571. [[CrossRef](#)]
90. Hart, S.R.; Hauri, E.H.; Oschmann, L.A.; Whitehead, J.A. Mantle Plumes and Entrainment: Isotopic Evidence. *Science* **1992**, *256*, 517–520. [[CrossRef](#)] [[PubMed](#)]
91. Pearce, J.A. Geochemical fingerprinting of oceanic basalts with applications to ophiolite classification and the search for Archean oceanic crust. *Lithos* **2008**, *100*, 14–48. [[CrossRef](#)]
92. Zhao, J.H.; Zhou, M.F. Geochemistry of Neoproterozoic mafic intrusions in the Panzhihua district (Sichuan Province, SW China): Implications for subduction related metasomatism in the upper mantle. *Precambrian Res.* **2007**, *152*, 27–47. [[CrossRef](#)]

93. Hirose, K.; Kushiro, I. Partial melting of dry peridotites at high pressures: Determination of compositions of melts segregated from peridotite using aggregates of diamond. *Earth Planet. Sci. Lett.* **1993**, *114*, 477–489. [[CrossRef](#)]
94. Shen, Y.; Scheirer, D.S.; Forsyth, D.W.; Macdonald, K.C. Trade-off in production between adjacent seamount chains near the East Pacific Rise. *Nature* **1995**, *373*, 140–143. [[CrossRef](#)]
95. Niu, Y.L.; Waggoner, D.G.; Sinton, J.M.; Mahoney, J.J. Mantle source heterogeneity and melting processes beneath seafloor spreading centres: The East Pacific Rise, 18°–19°S. *J. Geophys. Res.* **1996**, *101*, 27711–27733. [[CrossRef](#)]
96. Hekiniana, R.; Francheteaub, J.; Armijoc, R.; Cogne, J.P.; Constantin, M.; Girardeau, J.; Hey, R.; Naar, D.F.; Searle, R. Petrology of the Easter microplate region in the South Pacific. *J. Volcanol. Geotherm. Res.* **1996**, *72*, 259–289. [[CrossRef](#)]
97. Taylor, B.; Martinez, F. Back-arc basin basalt systematics. *Earth Planet. Sci. Lett.* **2003**, *210*, 481–497. [[CrossRef](#)]
98. O'Hara, M.J.; Richardson, S.W.; Wilson, G. Garnet-peridotite stability and occurrence in crust and mantle. *Contrib. Mineral. Petrol.* **1971**, *32*, 48–68. [[CrossRef](#)]
99. Klemme, S.; O'Neill, H.S.C. The near-solidus transition from garnet lherzolite to spinel lherzolite. *Contrib. Mineral. Petrol.* **2000**, *138*, 237–248. [[CrossRef](#)]
100. Wang, K.; Plank, T.; Walker, J.D.; Smith, E.I. A mantle melting profile across the Basin and Range, SW USA. *J. Geophys. Res.* **2002**, *107*, ECV-5. [[CrossRef](#)]
101. Plank, T.; Langmuir, C.H. The chemical composition of subducting sediment and its consequences for the crust and mantle. *Chem. Geol.* **1998**, *145*, 325–394. [[CrossRef](#)]
102. Thompson, R.N.; Morrison, M.A.; Hendry, G.L.; Parry, S.J. An Assessment of the Relative Roles of Crust and Mantle in Magma Genesis: An Elemental Approach. *Philos. Trans. R. Soc. A-Math. Phys. Sci.* **1984**, *310*, 549–590. [[CrossRef](#)]
103. Alibert, C. Mineralogy and geochemistry of a basalt from Site 738: Implications for the tectonic history of the southernmost part of the Kerguelen Plateau. In *Proceedings of the Ocean Drilling Program, Scientific Results*; Barron, J., Larsen, B., Eds.; Publications Distribution Center: Texas, TX, USA, 1991; pp. 293–297.
104. Mahoney, J.J.; Jones, W.B.; Frey, F.A.; Salters, V.J.M.; Pyle, D.G.; Davies, H.L. Geochemical characteristics of lavas from Broken Ridge, the Naturaliste Plateau and southernmost Kerguelen Plateau: Cretaceous plateau volcanism in the southeast Indian Ocean. *Chem. Geol.* **1995**, *120*, 315–345. [[CrossRef](#)]
105. Frey, F.A.; Mcnaughton, N.J.; Nelson, D.R.; deLaeter, J.R.; Duncan, R.A. Petrogenesis of the Bunbury Basalt, Western Australia: interaction between the Kerguelen plume and Gondwana lithosphere? *J. Afr. Earth Sci.* **1996**, *26*, 519–522. [[CrossRef](#)]
106. Albarède, F. *Introduction to Geochemical Modeling*; Cambridge University Press: Cambridge, UK, 1996.
107. Salters, V.J.M.; White, W.M. Hf isotope constraints on mantle evolution. *Chem. Geol.* **1998**, *145*, 447–460. [[CrossRef](#)]
108. Hoernle, K.A.J. Geochemistry of Jurassic oceanic crust beneath Gran Canaria (Canary Islands): Implications for crustal recycling and assimilation. *J. Petrol.* **1998**, *39*, 859–880. [[CrossRef](#)]
109. St. Weaver, B. Helena Revisited: Characteristics and Origin of the Type HIMU OIB. In *Proceedings of the AGU Fall Meeting, San Francisco, CA, USA, 11–15 December 2006*.
110. Schilling, J.G.; Thompson, G.; Kingsley, R.; Humphris, S. Hotspot-migrating ridge interaction in the South Atlantic. *Nature* **1985**, *313*, 187–191. [[CrossRef](#)]
111. Mahoney, J.; LeRoex, A.P.; Peng, Z.; Fisher, R.L.; Natland, J.H. Southwestern limits of Indian Ocean Ridge mantle and the origin of low ²⁰⁶Pb/²⁰⁴Pb mid-ocean ridge basalt: isotope systematics of the central southwest Indian Ridge (17°–50°E). *J. Geophys. Res.* **1992**, 19771–19790. [[CrossRef](#)]
112. Saunders, A.D.; Storey, M.; Kent, R.W.; Norry, M.J. Consequences of plume-lithosphere interaction. *Geol. Soc. Lond. Spec. Publ.* **1992**, *68*, 41–60. [[CrossRef](#)]

